Accepted Manuscript

Microwave dielectric properties of temperature stable MO-ZrO_2-Ta_2O_5 ceramics

Yun Zhang, Shihua Ding, Tianxiu Song, Yingchun Zhang

PII: S0925-8388(19)31933-4

DOI: https://doi.org/10.1016/j.jallcom.2019.05.251

Reference: JALCOM 50783

To appear in: *Journal of Alloys and Compounds*

Received Date: 30 January 2019

Revised Date: 19 May 2019

Accepted Date: 21 May 2019

Please cite this article as: Y. Zhang, S. Ding, T. Song, Y. Zhang, Microwave dielectric properties of temperature stable MO-ZrO_2-Ta_2O_5 ceramics, *Journal of Alloys and Compounds* (2019), doi: https://doi.org/10.1016/j.jallcom.2019.05.251.

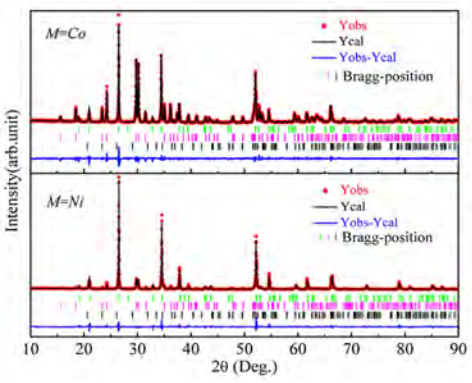

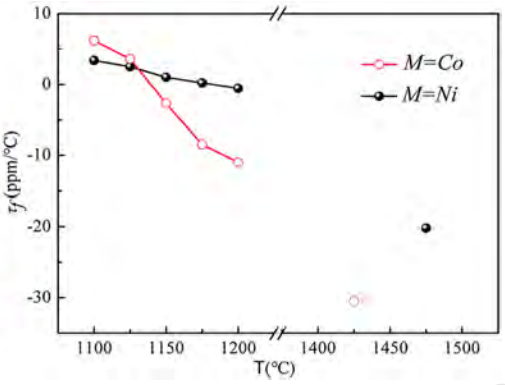

Microwave dielectric properties of temperature stable $MO\text{-}ZrO_2\text{-}Ta_2O_5$ ceramics

Yun Zhang[1*], Shihua Ding[1], Tianxiu Song[1], Yingchun Zhang[2]

1 School of Materials Science and Engineering, Xihua University, Chengdu, PR China

2 School of Materials Science and Engineering, University of Science and Technology Beijing, Beijing, P. R. China

[*] Corresponding author

E-mail address: yunzhang_17@163.com (Y. Zhang)

Fax:+86-03128152792; Tel:+86-03128152792

ABSTRACT

Temperature stable MO-ZrO_2-Ta_2O_5 ceramics (M=Co, Ni) were prepared by solid state route. Crystal structure was determined by X-ray diffraction and Raman spectrum. Single-phase $MZrTa_2O_8$ was formed through the reaction between intermediate MTa_2O_6 and residual ZrO_2. Quantitative phase analysis verified that changing temperature considerably adjusted the chemical compositions of ceramics. In the case of $CoZrTa_2O_8$, the optimum dielectric properties were ε_r~24.3, $Q\times f$~95,300 GHz (Q~11,305 at 8.43 GHz), and τ_f~-30.50 ppm/°C. The $NiZrTa_2O_8$ ceramic had ε_r=23.5, $Q\times f$=86,404 GHz (Q~10,774 at 8.02 GHz), and τ_f=-20.20 ppm/°C. Their large τ_f values were compensated since $MZrTa_2O_8$ and MTa_2O_6 had opposite τ_f. Particularly, near zero τ_f of -2.67 and 0.22 ppm/°C were obtained for M=Co, Ni at 1150 and 1175 °C, respectively.

Keywords

MO-ZrO_2-Ta_2O_5 ceramics; Microwave dielectric property; Phase composition

1. Introduction

The rapid development of modern society creates a high demand for electronic components. Many organics have been developed and modified, according to the specific needs [1-9]. Microwave dielectric ceramic is the resonance element and receives considerable attention in wireless telecommunication [10]. An effective dielectric ceramic must has (*i*) appropriate dielectric constant ε_r, (*ii*) low dielectric loss (or high quality factor $Q\times f$, where $Q=1/\tan\delta$) to decrease signal attenuation, and (*iii*) near-zero temperature dependence of resonant frequency, τ_f, to minimize frequency drift [11]. Recently, many kinds of novel low-ε_r microwave dielectrics are explored, such as olivine $LiMPO_4$ (M = Mg, Zn, Mn, Ni; ε_r=5.3~11.49, $Q\times f$=10,792~79,100 GHz) [12], $Ln_2Zr_3(MoO_4)_9$ (Ln=Sm, Nd, La, Eu; ε_r=10.8~11, $Q\times f$=50,628~74,900 GHz) [13], and cuspidine $Ca_3MSi_2O_9$ (M=Zr, Hf; ε_r=8.5~12.5, $Q\times f$=30,000~75,000 GHz) [14]. There is a renewed interest in V-based materials owing to the low sintering temperature, including $Ba_3M(V_2O_7)_2$ (M=Mg, Zn) [15], $Ba_2LnV_3O_{11}$ (Ln=Bi, La, Nd, Sm) [16], $AgCa_2M_2V_3O_{12}$ (M = Mg, Zn) [17]. The low ε_r together with desirable dielectric properties makes them promising candidates as millimeter-wave components. However, the drive for miniaturized devices requires new ceramics having higher ε_r.

A(Ti, Zr)Nb_2O_8 (A=Mg, Ca, Mn, Co, Ni, Zn) compounds have been widely studied due to their optical, photocatalytic and dielectric properties [18-20]. Tseng *et al.* [21, 22] reported that $ATiNb_2O_8$ (A=Co, Ni, Zn) system possessed medium ε_r about 37.4-64. Different dopings, such as Al_2O_3, Ta_2O_5 and ZrO_2, resulted in enhanced $Q\times f$

and large τ_f [23-25]. Li_2O-B_2O_3-SiO_2 glass lowered the sintering temperature of $ZnTiNb_2O_8$ to 850 °C [26]. Unfortunately, second phase was formed, along with rapid deterioration in $Q\times f$. As to $AZrNb_2O_8$ ceramics, Murthy [27] described the relationships between dielectric properties and crystal structure several years ago. For the purpose of optimization, numerous studies were conducted on them by utilizing kinds of substituents [28-31]. For instance, Zhang [28] reported that a small amount of Ta substitution promoted the $Q\times f$ of $ZnZrNb_2O_8$ to 75,800 GHz. 0.08 mol Sb^{5+} also remarkably enlarged the $Q\times f$ of $MgZrNb_2O_8$ ceramic [30]. The reasons could be explained from the view of complex bond theory, while the high sintering temperatures were still not satisfactory. Li [32, 33] further gained ultra-low loss $AZrTa_2O_8$ (A=Mg, Zn) ceramics ($Q\times f$~110,700-140,900 GHz). Based on this, Wang [34] in 2018 investigated the $CoZrTa_2O_8$ microwave ceramics. Nevertheless, all these Ta-containing dielectrics had been densified at 1250-1450 °C, accompanied by negative τ_f. Preliminary experiments indicated that good dielectric properties and excellent sintering behavior were difficult to obtain at the same time.

Our previous study shown that the formation of phase-pure $CoTiNb_2O_8$ was a multistep process [20]. CoO was always first reacted with Nb_2O_5 to form $CoNb_2O_6$. This intermediate phase then transformed to the final product by further heating. And the degree of phase transformation mainly depended on the temperature. $CoTiTa_2O_8$ also exhibited similarities in its synthesis [25]. It was reasonable to conclude that $CoTa_2O_6$ would be formed during $CoZrTa_2O_8$ formation. So the τ_f was able to be compensated at lower temperatures since they had opposite τ_f [34-36].

Considering the similar radius of Ni with Co, $NiZrTa_2O_8$ might also have negative τ_f. Meanwhile, the τ_f of $NiTa_2O_6$ was +35 ppm/°C [35, 36]. MTa_2O_6 (M=Co, Ni), in particular, exhibited high $Q\times f$ values (29,000~31,000 GHz). Thus, this stimulated us to seek temperature stable ceramics in the low loss $MO\text{-}ZrO_2\text{-}Ta_2O_5$ (M=Co, Ni) systems by changing temperature. The influence of chemical composition on the microwave dielectric properties was discussed in the succeeding sections.

2. Experimental procedures

$MO\text{-}ZrO_2\text{-}Ta_2O_5$ (M=Co, Ni) ceramics were prepared separately through solid-state route. The raw materials adopted were high-purity CoO (99.9%; Aladdin, Shanghai, China), NiO (99.9%; Aladdin, Shanghai, China), ZrO_2 (99.9%, Sinopharm Chemical Reagent Co. Ltd., Beijing, China), and Ta_2O_5 (99.99%, Zhu Zhou Harden Alloys Co. Ltd. Hunan, China). They were stoichiometrically weighed and ball milled in distilled water. The slurries were then dried and passed through a 200 mesh screen. The resultant powders were subsequently heat-treated at 950 °C for a duration of 4 h. After an intermediate grinding and sieving, they were ground thoroughly with 5 wt.% polyvinyl alcohol solution. The mixture were cold isostatically pressed into cylindrical specimens (10 mm in diameter and 6 mm in thickness) under 200 MPa. The samples were sintered at 1100-1200 °C and 1400-1500 °C.

The relative densities were determined as a ratio of bulk densities to theoretical densities. The bulk densities of sintered samples were analyzed by Archimedes method. The theoretical densities were calculated from the following equation:

$$\rho = \frac{w_1 + w_2 + w_3}{w_1/\rho_1 + w_2/\rho_2 + w_3/\rho_3} \quad (1)$$

where ρ_1, ρ_2 and ρ_3 were the theoretical density of $MZrTa_2O_8$, MTa_2O_6, and ZrO_2, w_1, w_2 and w_3 were the weight fraction of $MZrTa_2O_8$, MTa_2O_6, and ZrO_2, respectively. X-ray technique (D2-PHASER, Bruker) with Cu*K*α radiation was utilized to check phase purity. Scanning electron microscopy (FEI, Quanta 250) and energy dispersive spectroscopy (EDS) were utilized to recorded the surface morphology and chemical composition, respectively. Pore size distributions were determined by BET analysis (TriStar 3020 II, Micromeritics) and Mercury porosimetry (AutoPore IV 9500, Micromeritics). The microwave dielectric properties were measured with a HP8720ES network analyzer using Hakki-Coleman's dielectric resonator method, as modified by Courney and Kobayashi *et al*. [37-39]. All measurements were made in 7-9 GHz at room temperature. The τ_f was obtained at temperatures from 20 to 80 °C and calculated by the relationship as follows:

$$\tau_f = \frac{f_2 - f_1}{f_1(T_2 - T_1)} \quad (2)$$

where f_1 and f_2 were the resonant frequency at T_1 and T_2, respectively.

3. Results and discussion

3.1 Relative density

Fig. 1 shows the relative densities of MO-Ta_2O_5-ZrO_2 ceramics with different sintering temperatures. In the multi-phase region, the relative densities increased linearly with temperature, and were measured to be in the range 92.50-95.20%. The ceramics contained only $MZrTa_2O_8$ phase at temperatures up to 1400 °C. At the same time, the relative densities displayed a typical increase-then-decrease variation. The maximum densities of the $CoZrTa_2O_8$ and $NiZrTa_2O_8$ ceramics were 96.41% at

1425 °C and 96.52% at 1475 °C, respectively.

3.2 Multiphase refinement and quantitative determination

Fig. 2 displays the X-ray diffraction (XRD) patterns of MO-ZrO_2-Ta_2O_5 ceramics. For the CoO-ZrO_2-Ta_2O_5 ceramics in Fig. 2 (a), the phases included monoclinic $CoZrTa_2O_8$ (PDF# 48-0328), tirutile $CoTa_2O_6$ (PDF# 32-0314), and trace level monoclinic ZrO_2 (PDF# 37-1484). It should be noted that increasing temperature gradually weakened the peak intensities of $CoTa_2O_6$ but strengthened those of $CoZrTa_2O_8$. To obtain single phase, the green compacts were sintered between 1400 and 1500 °C. All recognizable reflection peaks could be readily indexed to monoclinic structure at the expense of $CoTa_2O_6$ and ZrO_2 [see Fig. 2 (c)]. Similar crystalline phase transition was identified in the NiO-ZrO_2-Ta_2O_5 system.

By means of GSAS program, Rietveld method was performed for quantitative phase analysis of the composites [40]. As representative examples, the refinement plots of MO-ZrO_2-Ta_2O_5 ceramics sintered at 1175 °C are shown in Fig. 3 (a). The lattice parameters derived from the refinements are listed in Tables 1 and 2. When M=Co, the content of $CoTa_2O_6$ decreased from 54.78 to 36.97 wt.% in the temperature range of 1100-1200 °C; whereas for $CoZrTa_2O_8$, it increased from 32.16 to 54.22 wt.% [Fig. 3 (b)]. While in the Ni-containing samples, the conversion of $NiTa_2O_6$ to $NiZrTa_2O_8$ was much slower than that of $CoTa_2O_6$. Thus, it could be concluded that $NiZrTa_2O_8$ synthesis needed more potent driving force.

The schematic crystal structures of $MZrTa_2O_8$, MTa_2O_6 and ZrO_2 are given in Fig. 3 (d). $CoTa_2O_6$ (or $NiTa_2O_6$) was reported to crystallize in the tetragonal structure

with space group *P*42/*mnm*. Here the cation sites were placed in an ordered fashion by Co (or Ni) and Ta ions [41]. In the structure of $MZrTa_2O_8$, M/Zr and Ta cations occupied 2*f* and 2*e* Wyckoff positions, respectively. Two different oxygen anions (O1 and O2) occupied 4*g* Wyckoff positions. O1 was connected to one Ta cation and two M/Zr cations, whereas O2 was bonded with one M/Zr-site and two Ta-site cations [27]. There were also two types of oxygen anions in baddeleyite. One was coordinated to three Zr atoms in an approximately planar configuration. And the other was four-coordinated in a distorted tetrahedral configuration [42].

3.3. Raman analysis

Fig. 4 presents the Raman shifts for $MO\text{-}ZrO_2\text{-}Ta_2O_5$ ceramics sintered at 1175 °C. According to the group theoretical calculation, the Raman-active modes of $MZrTa_2O_8$, MTa_2O_6 and ZrO_2 could be respectively determined as follows [43-45]:

$$\Gamma_1=9A_g+12B_g \quad (3)$$

$$\Gamma_2=4A_{1g}+2A_{2g}+2B_{1g}+4B_{2g}+6E_g \quad (4)$$

$$\Gamma_3=9A_g+8B_g \quad (5)$$

Experimentally, only a part of the vibration modes were obtained since some were broadened and overlapped. For the $CoO\text{-}ZrO_2\text{-}Ta_2O_5$ system, three main modes were attributed as follows: 179 cm^{-1} to Zr-O stretching vibration [46]; 380 cm^{-1} to CoO_6 octahedra stretching deformation; and a broad band at 600-700 cm^{-1} to Ta-O symmetric vibration [47]. The high frequency band at 859 cm^{-1} was also indexed to Ta-O symmetric vibration [48]. The very weak peaks near 239 cm^{-1} and 279 cm^{-1} were assigned to O-Ta-O bending. While the 475 cm^{-1} mode stemmed from Ta-O

stretching. ZrO_2 exhibited its characteristic mode at approximately 561 cm^{-1} [49]. The remaining two modes arose from the combination of O-Zr-O bending and symmetric vibration [43, 50].

When M=Ni, CoO_6 vibrational modes were absent and a medium intense band appeared at 413 cm^{-1} corresponding to Ni-O stretching mode [51]. Moreover, the broad bands in the region of 600-700 cm^{-1} moved to higher wave number side (see inset of Fig. 4). When Co was replaced by Ni, the unit cell volume decreased which in turn affected the interatomic distance and bond covalency in TaO_6 octahedron [52]. Out of these effects, the B_{1g} modes were red shifted. Beyond that, the intensity increased significantly in Ni-containing sample. This was because the large content of $NiTa_2O_6$ as well as enhanced structural symmetry.

3.4. Morphological analysis

Fig. 5 depicts the SEM micrographs of MO-Ta_2O_5-ZrO_2 ceramics sintered at various temperatures. The most remarkable microstructural change was the pore size distribution. At 1125 °C, the microstructure was granular like with a large amount of porosity, especially when M=Ni. As temperature increased, densification improved with steadily diminishing porosity. EDS microanalysis was carried out to attempt to distinguish the morphologies of $MZrTa_2O_8$, MTa_2O_6 and ZrO_2. However, based on the EDS spectrums (Fig. 6) and elemental compositions (inset of Fig. 5), all the selected areas displayed predominant distribution of M, Zr and Ta with a 1:1:2 molar ratio. This indicated the uniform diffusion of ions in MO-Ta_2O_5-ZrO_2 composites. Polygon shaped microstructures were generated at temperatures high enough to produce

single-phase ceramics. Here intergranular pores were removed and there was no evidence of pore entrapment. Densification occurred simultaneously at respective optimum sintering temperatures. Less porosity with homogeneous structures implied successful sintering of $MZrTa_2O_8$ ceramics.

The mesoporous nature of MO-Ta_2O_5-ZrO_2 samples is confirmed by BET measurements. The isotherms for low-pressure N_2 adsorption/desorption analyses are illustrated in Fig. 7 (a)-(d). Because of capillary condensation, there was a small closed hysteresis loop for NiO-Ta_2O_5-ZrO_2 sample sintered at 1175 °C. This loop could be classified as type H_3, which was usually associated with slit-shaped pores. As suggested by Groen [53], the BJH adsorption branch was taken for the calculation of pore size distribution. From the insets, it was observed that the distributions consisted mostly of primary mesoporous. Besides, the NiO-ZrO_2-Ta_2O_5 ceramic sintered at 1175 °C exhibited a large volume of macropores in the 200-250 nm range. The SEM in Fig. 5 demonstrated that the MO-Ta_2O_5-ZrO_2 samples also had micrometer-scale porosity. So Mercury porosimetry was introduced to further visualize the pores, and the results were presented in Fig. 7 (e). The micropore distribution of CoO-Ta_2O_5-ZrO_2 was bimodal with a definitive peak at around 140 mm and a small broad peak between 2 and 3 μm. When M=Ni, the pore size population shifted to larger values, as seen from Fig. 7 (f). These results were consistent with the SEM observations.

3.5 Microwave dielectric properties

Fig. 8 list the ε_r and $Q\times f$ of MO-ZrO_2-Ta_2O_5 (M=Co, Ni) ceramics as a function of

sintering temperature. The ε_r variations of pure $CoZrTa_2O_8$ and $NiZrTa_2O_8$ ceramics were in good agreement with the relative densities. The probable explanation was that the porous materials contained air as secondary phase (ε_r=1). The lower porosity, the superior ε_r would be. However, the ε_r of $CoO\text{-}ZrO_2\text{-}Ta_2O_5$ composite ($NiO\text{-}ZrO_2\text{-}Ta_2O_5$) decreased linearly from 29.0 to 27.1 (27.8 to 26.3) at 1100-1200 °C, even with enhanced sintering behavior. For multiphase dielectrics, the ε_r was dominated by the Lichtenecher rule rather than porosity [54]. The ε_r for $CoTa_2O_6$ and ZrO_2 was 29 and 36, respectively [35, 36, 55]. While it was 24.3 for $CoZrTa_2O_8$ ceramic, sintered at 1425 °C /4 h. As supported by XRD results, increasing temperature promoted the formation of $CoZrTa_2O_8$, thereby reducing the ε_r.

In contrast to ε_r, the $Q\times f$ in multi-phase region increased initially. This might be because the effect of polarization at the pore surfaces was minimized [56]. The absence of moisture in the samples also gave rise to possible loss mechanism. Another reason for the dielectric loss reduction was the relatively higher $Q\times f$ value of $MZrTa_2O_8$ than MTa_2O_6 and ZrO_2. It is generally known that extrinsic phenomena such as porosity will cause deviation from the intrinsic dielectric properties of materials. A low level of porosity (<5%) decreases the $Q\times f$ but doesn't have a major influence. According to Fig. 1, the ceramics sintered at 1400-1500 °C were highly densified, allowing the effects of porosity to be ignored. Thus, further investigations are needed to evaluate the intrinsic loss. When compared with $NiZrTa_2O_8$, $CoZrTa_2O_8$ ceramic had less dielectric loss and hence yielded greater $Q\times f$ values in the final $MO\text{-}ZrO_2\text{-}Ta_2O_5$ composite. To be noted that the $Q\times f$ of $CoZrTa_2O_8$ reported here was

up to 95,300 GHz, but very different from a recent report [34]. In practice, the microwave dielectric properties of materials differed, depending on the starting materials, preparation conditions, and so forth. For instance, the $Q\times f$ of $CoZrNb_2O_8$ had been reported as 26,950 GHz by Murthy [27], 4,7100 GHz by Wu [43], and 97,830 GHz by zhang *et al*. [57]. Additionally, the Q of $CoNb_2O_6$ in [58] was at least twice that gave by Lee *et al*. [59]. The frequency dependence of dielectric loss was also discussed in this work. For measurement, the frequency was tuned by changing the sample size. The quality factor Q of microwave dielectric ceramic, is approximately equal to 1/tanδ. Q will decrease with increasing frequency f, and the theory is that the $Q\times f$ is a constant [60]. This rule has been widely accepted for decades. Thus, $Q\times f$ is usually used to describe the dielectric property instead of tanδ. As seen from Fig. 9, all materials demonstrated linearity in their dielectric losses, conforming to the $Q\times f$-constant rule.

Amongst the three important characteristics, the τ_f is the least sensitive to porosity. The measured τ_f values in Fig. 10 ranged from 6.20 to -10.99 ppm/°C for CoO-ZrO_2-Ta_2O_5 and 3.41 to -0.54 ppm/°C for NiO-ZrO_2-Ta_2O_5. The τ_f of $CoTa_2O_6$ and $NiTa_2O_6$ was 24 and 26 ppm/°C, respectively [35]. Some of the earlier study [55] shown that ZrO_2 might have a positive τ_f. On the contrast, the $CoZrTa_2O_8$ and $NiZrTa_2O_8$ both possessed negative τ_f values in the present work. Thus, there was a possibility to tailor the τ_f by chemical composition variation and, more specifically, by temperature change. A near zero τ_f of -2.67 ppm/°C was obtained in the CoO-ZrO_2-Ta_2O_5 ceramic with ε_r~28.2 and $Q\times f$~70,562 GHz. In the case of

NiO-ZrO_2-Ta_2O_5, the composite sintered at 1175 °C/4 h had ε_r~26.7, $Q\times f$~57,127 GHz and τ_f 0.22 ppm/°C.

Compared with the pure phase $MZrTa_2O_8$ ceramics, MO-ZrO_2-Ta_2O_5 composites exhibited comparatively lower ε_r and $Q\times f$. The above analyses shown that one of the important contributions to dielectric property was the densification. Thus, porosity correction was used to evaluate what the dielectric property of fully dense ceramics would be. The permittivity was corrected using [61]

$$\varepsilon_{meas} = \varepsilon_{corr}\left(1-\frac{3P(\varepsilon_{corr}-1)}{2\varepsilon_{corr}+1}\right) \quad (6)$$

where P was the porosity fraction, ε_{meas} and ε_{corr} were the measured and corrected permittivity, respectively. According to this equation, the ε_{corr} for CoO-ZrO_2-Ta_2O_5 and NiO-ZrO_2-Ta_2O_5 ceramics were 30.7 at 1150 °C and 29.2 at 1175 °C, respectively. The full density dielectric quality factor could be estimated using the relationship [61]

$$\frac{1}{Q}=(1-P)\frac{1}{Q_0}+A'P\left(\frac{P}{1-P}\right)^{2/3} \quad (7)$$

where Q_0 was the full density dielectric quality factor, A' was a constant, and P was the porosity. This approach also gave substantially larger $Q_0\times f$ of 198,642 GHz (M=Co, Q_0~22,991 at 8.64 GHz) and 142,623 GHz (M=Ni, Q_0~18,008 at 7.92 GHz) firing at 1150 and 1175 °C, respectively. Thus, temperature stable MO-ZrO_2-Ta_2O_5 ceramics with dense microstructure will be prepared by other techniques, such as hot-pressing-sintering.

4. Conclusions

The effects of processing parameters on the crystal structure and microwave dielectric properties of MO-ZrO_2-Ta_2O_5 ceramics were discussed systematically. XRD

results demonstrated that $MZrTa_2O_8$ phase was formed through the chemical reaction of intermediate MTa_2O_6 with ZrO_2. Available data suggested that the presence of reaction intermediate had a significant effect on the dielectric properties. The maximum $Q \times f$ values of 95,300 and 86,404 GHz were obtained for $CoZrTa_2O_8$ and $NiZrTa_2O_8$ ceramics as sintered individually at 1425 and 1475 °C. Additionally, their large τ_f values were compensated by chemical composition changes. For CoO-ZrO_2-Ta_2O_5 sintered at 1150 °C /4 h, the dielectric properties were ε_r~28.2, $Q \times f$~70,562 GHz (Q~8,167 at 8.64 GHz), and τ_f~-2.67 ppm/°C. The NiO-ZrO_2-Ta_2O_5 composite showed ε_r~26.7, $Q \times f$~57,127 GHz (Q~7,213 at 7.92 GHz), and τ_f~0.22 ppm/°C at 1175 °C /4 h.

Acknowledgments

This work has been supported by Xihua University Talents Supporting Program (Grant No. 21030028), the Sichuan Science and Technology Program (Grant No. 19ZDYF0908).

References

[1] X. F. Chen, Y. Huang, X. P. Han, K. C. Zhang, Synthesis of cobalt nanofibers@ nickel sulfide nanosheets hierarchical core-shell composites for anode materials of lithium ion batteries, Electrochim. Acta 284 (2018) 418-426.

[2] X. F. Chen, Y. Huang, K. C. Zhang, Cobalt nanofibers coated with layered nickel silicate coaxial core-shell composites as excellent anode materials for lithium ion batteries, J. Colloid Interface Sci. 513 (2018) 788-796.

[3] X. F. Chen, Y. Huang, K. C. Zhang, W. C. Zhang, Cobalt fibers anchored with tin disulfide nanosheets as high-performance anode materials for lithium ion batteries, J. Colloid Interface Sci. 506 (2017) 291-299.

[4] X. F. Chen, Y. Huang, K. C. Zhang, X. S. Feng, M. Y. Wang, Porous TiO_2 nanobelts coated with mixed transition-metal oxides Sn_3O_4 nanosheets core-shell composites as high-performance anode materials of lithium ion batteries, Electrochim. Acta 259 (2018) 131-142.

[5] H. Lv, Z. Yang, P. Wang, G. Ji, J. Song, L. Zheng, H. Zeng, Z. Xu, A voltage-boosting strategy enabling a low-frequency, flexible electromagnetic wave absorption device, Adv. Mater. 30 (2018) 1706343-1706350.

[6] H. L. Lv, Z. H. Yang, S. J. H. Ong, C. Wei, H. B. Liao, S. B. Xi, Y. H. Du, G. B. Ji, Z. J. Xu, A flexible microwave shield with tunable frequency-transmission and electromagnetic compatibility, Adv. Funct. Mater. (2019) https://doi.org/10.1002/adfm.201900163.

[7] G. L. Wu, H. X. Zhang, X. X. Luo, L. J. Yang, H. L. Lv, Investigation and

optimization of Fe/$ZnFe_2O_4$ as a wide-band electromagnetic absorber, J. Colloid Interface Sci. 536 (2019) 548-555.

[8] B. Zhao, Y. Li, J. Liu, L. Fan, K. Gao, Z. Bai, L. Liang, X. Guo, R. Zhang, Symmetrical polyhedron-bowl Co/CoO with hexagonal plate to forward electromagnetic wave absorption ability, Cryst. Eng. Commun. 21 (2019) 816-826.

[9] H. L. Lv, X. H. Liang, Y. Cheng, H. Q. Zhang, D. M. Tang, B. S. Zhang, G. B. Ji, Y. W. Du, Coin-like α-Fe_2O_3@$CoFe_2O_4$ core-shell composites with excellent electromagnetic absorption performance, ACS Appl. Mater. Interfaces 7 (2015) 4744-4750.

[10] M. T. Sebastian, Dielectric materials for wireless communication, Elsevier Science Publishers, Oxford, 2008.

[11] C. F. Tseng, H. C. Hsu, P. H. Chen, Microwave dielectric properties of $Li_2W_2O_7$ ceramics improved by Al_2O_3 addition, J. Alloys Compd. 764 (2018) 840-844.

[12] P. Zhang, S. X. Wu, M. Xiao, The microwave dielectric properties and crystal structure of low temperature sintering $LiNiPO_4$ ceramics, J. Eur. Ceram. Soc. 38 (2018) 4433-4439.

[13] Y. H. Zhang, J. J. Sun, N. Dai, Z. C. Wu, H. T. Wu, C. H. Yang, Crystal structure, infrared spectra and microwave dielectric properties of novel extra low-temperature fired $Eu_2Zr_3(MoO_4)_9$ ceramics, J. Eur. Ceram. Soc. 39 (2019) 1127-1131.

[14] X. Q. Song, K. Du, X. Z. Zhang, J. Li, W. Z. Lu, X. C. Wang, W. Lei, Crystal structure, phase composition and microwave dielectric properties of $Ca_3MSi_2O_9$ ceramics, J. Alloys Compd. 750 (2018) 996-1002.

[15] R. Naveenraj, E. K. Suresh, J. Dhanya, R. Ratheesh, Preparation and microwave dielectric properties of $Ba_3A(V_2O_7)_2$ (A=Mg, Zn) ceramics for ULTCC applications, Eur. J. Inorg. Chem. 2019 (2019) 949-955.

[16] C. C. Li, H. C. Xiang, M. Y. Xu, J. Khaliq, J. Q. Chen, L. Fang, Low□firing and temperature stable microwave dielectric ceramics: $Ba_2LnV_3O_{11}$ (Ln=Nd, Sm), J. Am. Ceram. Soc. 101 (2018) 773-781.

[17] J. Q. Chen, Y. Tang, H. C. Xiang, L. Fang, H. Porwal, C. C. Li, Microwave dielectric properties and infrared reflectivity spectra analysis of two novel low-firing $AgCa_2B_2V_3O_{12}$ (B=Mg, Zn) ceramics with garnet structure, J. Eur. Ceram. Soc. 38 (2018) 4670-4676.

[18] N. Kumada, N. Koike, K. Nakanome, S. Yanagida, T. Takei, A. Miura, Synthesis of rutile-type solid solution $Ni_{1-x}Co_xTi(Nb_{1-y}Ta_y)_2O_8$ ($0\leq x\leq 1$, $0\leq y\leq 1$) and its optical property, J. Asian Ceram. Soc. 5 (2017) 284-289.

[19] N. Kumada, K. Nakanome, S. Yanagida, T. Takei, I. Fujii, S. Wada, Crystal structure, photocatalytic and dielectric property of $ATiM_2O_8$ (A: Mg, Zn; M: Nb, Ta), J. Asian Ceram. Soc. 6 (2018) 247-253.

[20] Y. Zhang, Y. C. Zhang, M. Q. Xiang, Low temperature sintering and microwave dielectric properties of $CoTiNb_2O_8$ ceramics with CuO addition, Ceram. Int. 42 (2016) 3542-3547.

[21] C. F. Tseng, Microwave dielectric properties of low loss microwave dielectric ceramics: $A_{0.5}Ti_{0.5}NbO_4$ (A=Zn, Co), J. Eur. Ceram. Soc. 34 (2014) 3641-3648.

[22] X. Huang, H. W. Zhang, Y. M. Lai, G. Wang, M. M. Li, C. Y. Hong, J. Li,

Relationship of crystal structure and microwave dielectric properties in $Ni_{0.5}Ti_{0.5}NbO_4$ ceramics with Ta substitution, Eur. J. Inorg. Chem. 17 (2018) 1800-1804.

[23] W. J. Luo, L. X. Li, S. H. Yu, J. N. Li, B. W. Zhang, J. L. Qiao, S. L. Chen, Bond theory, terahertz spectra, and dielectric studies in donor□acceptor (Nb□Al) substituted $ZnTiNb_2O_8$ system, J. Am. Ceram. Soc. (2019) https://doi.org/10.1111/jace.16318.

[24] Y. J. Huang, Y. M. Li, Z. M. Wang, Z. X. Xie, Z. Y. Shen, Y. Hong, Effects of Zr substitution on microstructure and microwave dielectric properties of $Zn(Ti_{1-x}Zr_x)Nb_2O_8$ ceramics, Appl. Phys. A 125 (2019) 29.

[25] H. Y. Yang, S. R. Zhang, Y. W. Chen, H. C. Yang, Y. Yuan, E. Z. Li, Crystal chemistry, Raman spectra, and bond characteristics of trirutile-type $Co_{0.5}Ti_{0.5}TaO_4$ microwave dielectric ceramics, Inorg. Chem. 58 (2018) 968-976.

[26] H. Y. Yang, E. Z. Li, H. C. Yang, H. C. He, S. R. Zhang, Synthesis of $Zn_{0.5}Ti_{0.5}NbO_4$ microwave dielectric ceramics with Li_2O□B_2O_3□SiO_2 glass for LTCC application, Int. J. Appl. Glass Sci. 9 (2018) 392-402.

[27] S. D. Ramarao, V. R. K. Murthy, Crystal structure refinement and microwave dielectric properties of new low dielectric loss $AZrNb_2O_8$ (A: Mn, Zn, Mg and Co) ceramics, Scr. Mater. 69 (2013) 274-277.

[28] P. Zhang, Y. G. Zhao, H. T. Wu, Bond ionicity, lattice energy, bond energy and microwave dielectric properties of $ZnZr(Nb_{1-x}A_x)_2O_8$ (A=Ta, Sb) ceramics, Dalton Trans. 44 (2015) 16684-16693.

[29] M. Xiao, J. Lou, Y. S. Wei, P. Zhang, Crystal structure and microwave dielectric

properties of $MgZr_{1-x}Sn_xNb_2O_8$ ceramics, Ceram. Int. 44 (2018) 885-889.

[30] M. Xiao, S. S. He, J. Lou, P. Zhang, Structure and microwave dielectric properties of $MgZr(Nb_{1-x}Sb_x)_2O_8$ ($0 \leq x \leq 0.1$) ceramics, J. Alloys Compd. 777 (2019) 350-357.

[31] M. Xiao, S. S. He, J. Lou, P. Zhang, Influence of Ge^{4+} substitution for Zr^{4+} on the microwave dielectric properties of $Mg(Zr_{1-x}Ge_x)Nb_2O_8$ ($0 \leq x \leq 0.4$) ceramics, Ceram. Int. 44 (2018) 21585-21590.

[32] X. S. Lyu, L. X. Li, S. Zhang, A new low-loss dielectric material $ZnZrTa_2O_8$ for microwave devices, J. Eur. Ceram. Soc. 36 (2016) 931-935.

[33] X. S. Lyu, L. X. Li, H. Sun, S. Zhang, S. Li, High-*Q* microwave dielectrics in wolframite magnesium zirconium tantalite ceramics, Ceram. Int. 42 (2016) 2036-2040.

[34] Y. Wang, S. B. Zhang, T. L. Tang, W. S. Xia, L. W. Shi, Investigation on microwave dielectric properties of new low-loss $CoZrTa_2O_8$ ceramics, Mater. Lett. 231 (2018) 1-4.

[35] E. S. Kim, C. J. Jeon, Crystal structure and microwave dielectric properties of $ATiO_3$, ATa_2O_6, AWO_4 (A=Ni, Mg, Co) ceramics, ISAF 2009, 18th IEEE International Symposium on the Applications of Ferroelectrics, 2009, 1-6.

[36] H. J. Lee, I. T. Kim, K. S. Hong, Dielectric properties of AB_2O_6 compounds at microwave frequencies (A=Ca, Mg, Mn, Co, Ni, Zn, and B=Nb, Ta), Jpn. J. Appl. Phys. 36 (1997) L1318-L1320.

[37] B. W. Hakki, P. D. Coleman, A dielectric resonator method of measuring

inductive capacities in the millimeter range, IRE Trans. Microw. Theory Tech. 8 (1960) 402-410.

[38] W. E. Courtney, Analysis and evaluation of a method of measuring the complex permittivity of microwave insulators, IEEE Trans. Microw. Theory Tech. 18 (1970) 476-485.

[39] Y. Kobayashiy, M. Katoh, Microwave measurement of dielectric properties of low-loss materials by the dielectric rod resonator method, IEEE Trans. Microw. Theory Tech. 33 (1985) 586-592.

[40] B. H. Toby, EXPGUI, a graphical user interface for GSAS, J. Appl. Crystallogr. 34 (2001) 210-213.

[41] E. J. Felten, P. G. Sprang, S. Rosen, Phase relations in the system $CoNb_2O_6$-$CoTa_2O_6$, J. Am. Ceram. Soc. 49 (1966) 273-276.

[42] D. K. Smith, W. Newkirk, The crystal structure of baddeleyite (monoclinic ZrO_2) and its relation to the polymorphism of ZrO_2, Acta Crystallogr. 18 (1965) 983-991.

[43] H. T. Wu, Z. B. Feng, Q. J. Mei, J. D. Guo, J. X. Bi, Correlations of crystal structure, bond energy and microwave dielectric properties of $AZrNb_2O_8$ (A=Zn, Co, Mg, Mn) ceramics, J. Alloys Compd. 648 (2015) 368-373.

[44] D. P. Xu, S. H. Gao, W. Q. Liu, Y. Liu, Q. Zhou, L. Li, T. Cui, H. M. Yuan, The Raman scattering of trirutile structure $MgTa_2O_6$ single crystals grown by the optical floating zone method, RSC Adv. 9 (2019) 839-843.

[45] V. G. Keramidas, W. B. White, Raman scattering study of the crystallization and phase transformations of ZrO_2, J. Am. Ceram. Soc. 57 (1974) 22-24.

[46] G. Murtaza, S. S. Hussain, N. U. Rehman, S. Naseer, M. Shafiq, M. Zakaullah, Carburizing of zirconium using a low energy mather type plasma focus, Surf. Coat. Technol. 205 (2011) 3012-3019.

[47] A. B. Cusick, M. Lang, F. Zhang, Amorphization of Ta_2O_5 under swift heavy ion irradiation, Nucl. Instrum. Meth. Phys. Res. Sect. B 407 (2017) 25-33.

[48] M. J. Wu, Y. C. Zhang, M. Q. Xiang, Structural, Raman spectroscopic and microwave dielectric studies on $(1-x)NiZrNb_2O_8$-$xZnTa_2O_6$, J. Mater. Sci.: Mater. Electron. 29 (2018) 14471-14478.

[49] C. M. Phillippi, K. S. Mazdiyasni, Infrared and Raman spectra of zirconia polymorphs, J. Am. Ceram. Soc. 54 (1971) 254-258.

[50] S. Solomon, A. George, J. K. Thomas, A. John, Preparation, characterization, and ionic transport properties of nanoscale $Ln_2Zr_2O_7$ (Ln=Ce, Pr, Nd, Sm, Gd, Dy, Er, and Yb) energy materials, J. Electron. Mater. 44 (2015) 28-37.

[51] T. Shao, Z. Qi, Y. Wang, Y. Li, M. Yang, C. Hu, Metal-insulator transition in epitaxial $NdNiO_3$ thin film: a structural, electrical and optical study, Appl. Surf. Sci. 399 (2017) 346-350.

[52] S. D. Ramarao, S. R. Kiran, V. R. K. Murthy, Structural, lattice vibrational, optical and microwave dielectric studies on $Ca_{1-x}Sr_xMoO_4$ ceramics with scheelite structure, Mater. Res. Bull. 56 (2014) 71-79.

[53] J. C. Groen, L. A. A. Peffer, J. Pérez-Ramírez, Pore size determination in modified micro- and mesoporous materials. Pitfalls and limitations in gas adsorption data analysis, Micropor. Mesopor. Mater. 60 (2003) 1-17.

[54] Y. G. Wu, X. H. Zhao, F. Li, Z. G. Fan, Evaluation of mixing rules for dielectric constants of composite dielectrics by MC-FEM calculation on 3D cubic lattice, J. Electroceram. 11 (2003) 227-239.

[55] X. S. Lv, L. X. Li, H. Sun, S. Li, S. Zhang, Microwave dielectric properties of novel temperature stable high *Q* $MgZr_{1+x}Nb_2O_{8+2x}$ ceramics, Ceram. Int. 41 (2015) 15287-15291.

[56] D. M. Iddles, A. J. Bell, A. J. Moulson, Relationships between dopants, microstructure and the microwave dielectric properties of ZrO_2-TiO_2-SnO_2 ceramics, J. Mater. Sci. 27 (1992) 6303-6310.

[57] Y. Zhang, Y. C. Zhang, M. Q. Xiang, Crystal structure and microwave dielectric characteristics of Zr-substituted $CoTiNb_2O_8$ ceramics, J. Eur. Ceram. Soc. 36 (2016) 1945-1951.

[58] R. C. Pullar, J. D. Breeze, N. M. Alford, Characterization and microwave dielectric properties of $M^{2+}Nb_2O_6$, J. Am. Ceram. Soc. 88 (2005) 2466-2471.

[59] H. J. Lee, K. S. Hong, S. J. Kim, I. T. Kim, Dielectric properties of MNb_2O_6 compounds (where M=Ca, Mn, Co, Ni, or Zn), Mater. Res. Bull. 32 (1997) 847-855.

[60] I. M. Reaney, Microwave dielectric ceramics for resonators and filters in mobile phone networks, J. Am. Ceram. Soc. 89 (2006) 2063-2072.

[61] S. J. Penn, N. M. N. Alford, A. Templeton, X. R. Wang, M. S. Xu, M. Reece, K. Schrapel, Effect of porosity and grain size on the microwave dielectric properties of sintered alumina, J. Am. Ceram. Soc. 80 (1997) 1885-1888.

Fig. 1 The relative densities of MO-ZrO_2-Ta_2O_5 ceramics

Fig. 2 XRD patterns of MO-ZrO_2-Ta_2O_5 ceramics sintered at (a-b) 1100-1200 °C and (c-d) 1400-1500 °C

Fig. 3 (a) Rietveld refinement plots of MO-ZrO_2-Ta_2O_5 samples sintered at 1175 °C; (b) Mass fraction of each phase for the CoO-ZrO_2-Ta_2O_5 ceramics; (c) Mass fraction of each phase for the NiO-ZrO_2-Ta_2O_5 ceramics; and (d) The schematic crystal structures of $MZrTa_2O_8$, MTa_2O_6 and ZrO_2

Fig. 4 The Lorentzian peak fit of the experimental Raman profile for (a) CoO-ZrO_2-Ta_2O_5 and (b) NiO-ZrO_2-Ta_2O_5 samples. The symbols are experimental points and the solid lines are fitted curves. Inset shows a magnified view of B_{1g} modes in the range 600-700 cm^{-1}

Fig. 5 SEM of (a_1-a_6) CoO-ZrO_2-Ta_2O_5 and (b_1-b_6) NiO-ZrO_2-Ta_2O_5 ceramics with the corresponding elemental composition

Fig. 6 EDS spectrums taken from MO-ZrO_2-Ta_2O_5 samples sintered at 1175 °C: (a-c) M=Co, (d-f) M=Ni. The detection of Au is due to gold coating for a better SEM observation

Fig. 7 (a-d) Pore size distributions of MO-ZrO_2-Ta_2O_5 samples determined by BET analysis; (e) Pore size distribution curves measured by Mercury porosimetry; (f) Magnified view of pore size distributions in (e)

Fig. 8 (a) ε_r and (b) $Q\times f$ of MO-ZrO_2-Ta_2O_5 ceramics sintered at various temperatures

Fig. 9 The frequency dependence of dielectric loss for MO-ZrO_2-Ta_2O_5 ceramics

Fig. 10 The τ_f values of sintered MO-ZrO_2-Ta_2O_5 ceramics

Table 1 Crystallograghic data obtained from Rietveld refinement for CoO-ZrO_2-Ta_2O_5 ceramics

T_s	Lattice parameters					V_{unit} (Å^3)	Reliability factors
	a (Å)	b (Å)	c (Å)	α=γ	β		R_{wp}(%), R_p(%), χ^2
(a) $CoTa_2O_6$							
1100	4.7338	4.7338	9.1811	90	90	205.7380	9.1, 8.2, 1.11
1125	4.7342	4.7342	9.1908	90	90	205.9902	9.4, 8.4, 1.12
1150	4.7329	4.7329	9.1971	90	90	206.0182	9.2, 8.6, 1.07
1175	4.7373	4.7373	9.2019	90	90	206.5091	9.3, 8.2, 1.13
1200	4.7474	4.7474	9.1924	90	90	207.1765	9.5, 8.4, 1.13
(b) $CoZrTa_2O_8$							
1100	4.7974	5.6551	5.1047	90	91.0355	138.4668	9.6, 8.3, 1.16
1125	4.8021	5.6542	5.1123	90	91.0234	138.7872	10.1, 8.3, 1.22
1150	4.7981	5.6564	5.1144	90	91.0441	138.7816	9.5, 8.3, 1.14
1175	4.8082	5.6421	5.1074	90	91.0326	138.5328	9.6, 8.4, 1.14
1200	4.8015	5.6418	5.1127	90	91.0554	138.4750	9.4, 8.3, 1.13
(c) ZrO_2							
1100	5.3119	5.2105	5.1471	90	99.2218	140.6184	9.4, 8.2, 1.15
1125	5.3121	5.2123	5.1473	90	99.2220	140.6777	9.7, 8.5, 1.14
1150	5.3107	5.2107	5.1507	90	99.2314	140.6866	10.1, 8.6, 1.17
1175	5.3201	5.2206	5.1504	90	99.2123	141.2028	9.8, 8.5, 1.15
1200	5.3129	5.2224	5.1571	90	99.2217	141.2400	9.8, 8.4, 1.17

R_{wp}-reliability factor of weighted pattern; R_p-reliability factor of patterns; χ^2-goodness of fit indicator

Table 2 Crystallograghic data obtained from Rietveld refinement for NiO-ZrO_2-Ta_2O_5 ceramics

T_s	Lattice parameters					V_{unit} (Å^3)	Reliability factors
	a (Å)	b (Å)	c (Å)	α=γ	β		R_{wp}(%), R_p(%), χ^2
(a) $NiTa_2O_6$							
1100	4.7218	4.7218	9.1411	90	90	203.8044	10.1, 8.7, 1.16
1125	4.7214	4.7214	9.1422	90	90	203.7944	9.6, 8.5, 1.13
1150	4.7226	4.7226	9.1502	90	90	204.0765	9.9, 8.9, 1.11
1175	4.7219	4.7219	9.1567	90	90	204.1609	10.2, 8.8, 1.16
1200	4.7217	4.7217	9.1678	90	90	204.3911	9.9, 8.5, 1.16
(b) $NiZrTa_2O_8$							
1100	4.7712	5.6462	5.0891	90	90.9355	137.0778	9.7, 8.2, 1.18
1125	4.7634	5.6567	5.0911	90	90.9495	137.1615	9.8, 8.3, 1.18
1150	4.7722	5.6598	5.0942	90	90.9782	137.5727	9.9, 8.6, 1.15
1175	4.7789	5.6592	5.0952	90	90.9782	137.7783	9.8, 8.7, 1.13
1200	4.7791	5.6598	5.0961	90	90.9892	137.8226	10.2, 8.7, 1.17
(c) ZrO_2							
1100	5.3111	5.2047	5.1277	90	99.2234	139.9108	10.4, 8.7, 1.13
1125	5.3141	5.2111	5.1389	90	99.2234	140.4681	10.1, 8.9, 1.13
1150	5.3131	5.2120	5.1398	90	99.2267	140.4892	9.8, 8.7, 1.13
1175	5.3127	5.2178	5.1427	90	99.2356	140.7107	9.9, 8.6, 1.15
1200	5.3126	5.2219	5.1528	90	99.2344	141.0957	9.9, 8.6, 1.15

R_{wp}-reliability factor of weighted pattern; R_p-reliability factor of patterns; χ^2-goodness of fit indicator

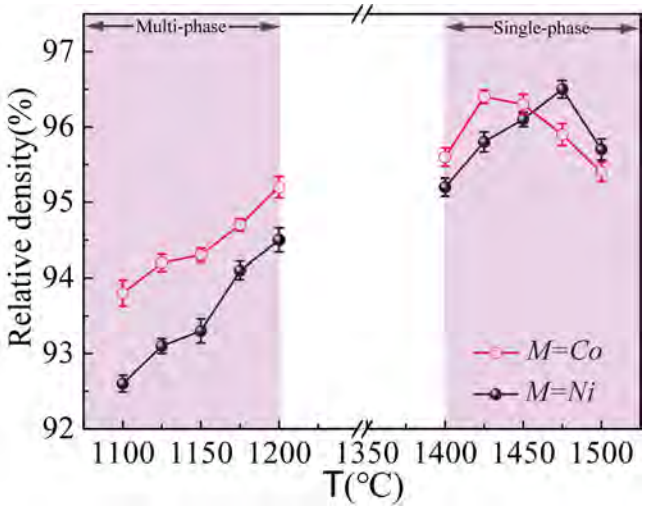

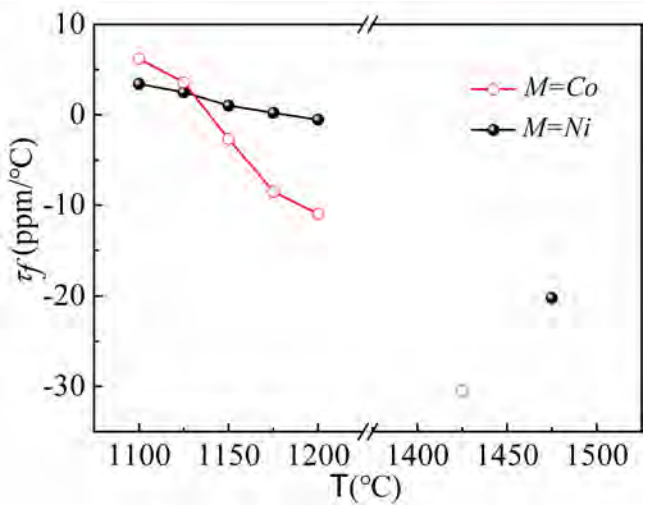

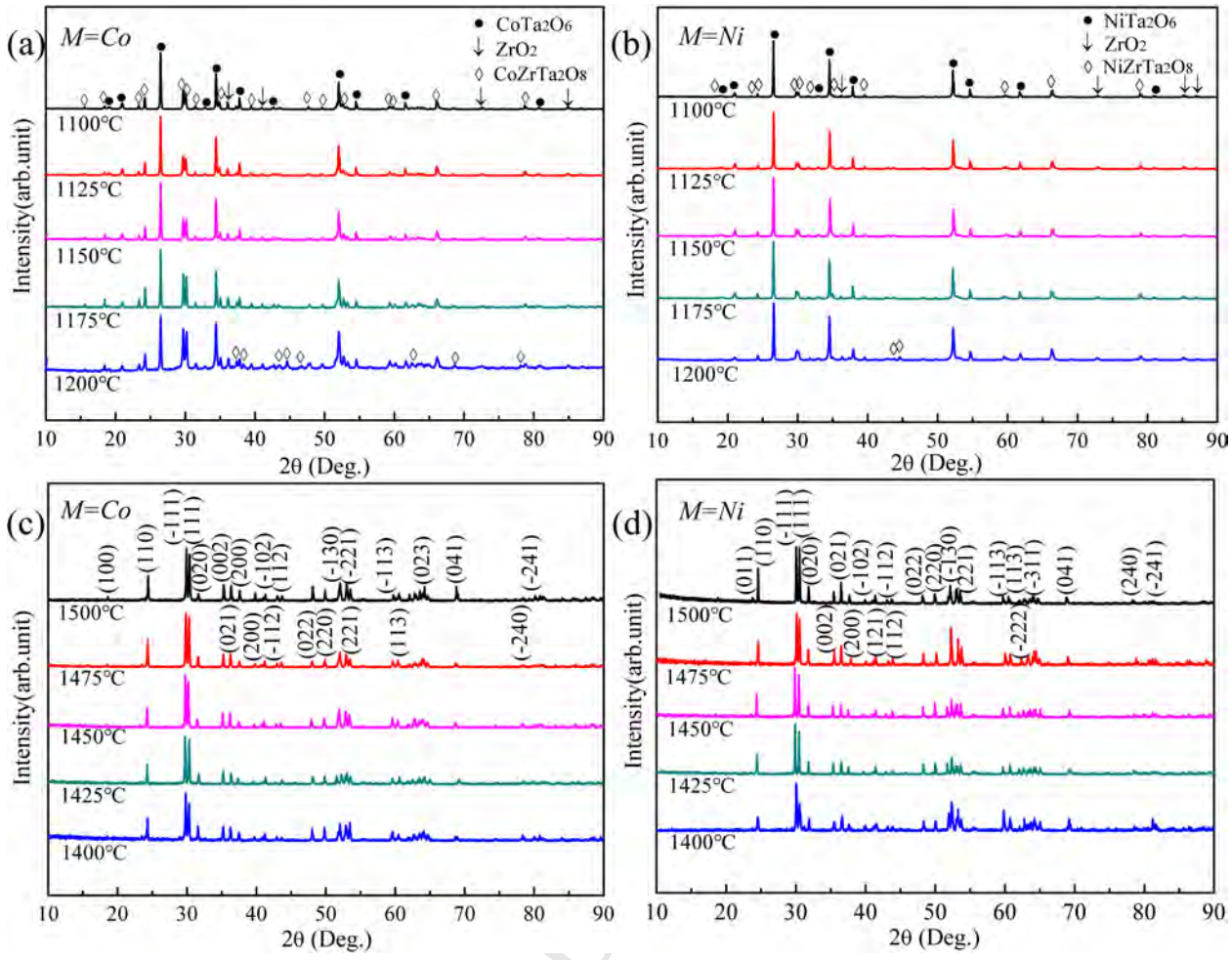
(a)
M=Co
CoTa2O6
ZrO2
CoZrTa2O8
1100°C
1125°C
1150°C
1175°C
1200°C
Intensity(arb.unit)
2θ (Deg.)
(b)
M=Ni
NiTa2O6
ZrO2
NiZrTa2O8
1100°C
1125°C
1150°C
1175°C
1200°C
Intensity(arb.unit)
2θ (Deg.)
(c)
M=Co
(100)
(110)
(-111)
(111)
(020)
(002)
(200)
(-102)
(-112)
(-130)
(-221)
(-113)
(023)
(041)
(-241)
(021)
(022)
(220)
(-240)
1500°C
1475°C
1450°C
1425°C
1400°C
Intensity(arb.unit)
2θ (Deg.)
(d)
M=Ni
(011)
(110)
(-111)
(111)
(020)
(021)
(-102)
(-112)
(022)
(220)
(-130)
(221)
(-113)
(113)
(-311)
(041)
(240)
(-241)
(002)
(200)
(121)
(112)
(-222)
1500°C
1475°C
1450°C
1425°C
1400°C
Intensity(arb.unit)
2θ (Deg.)

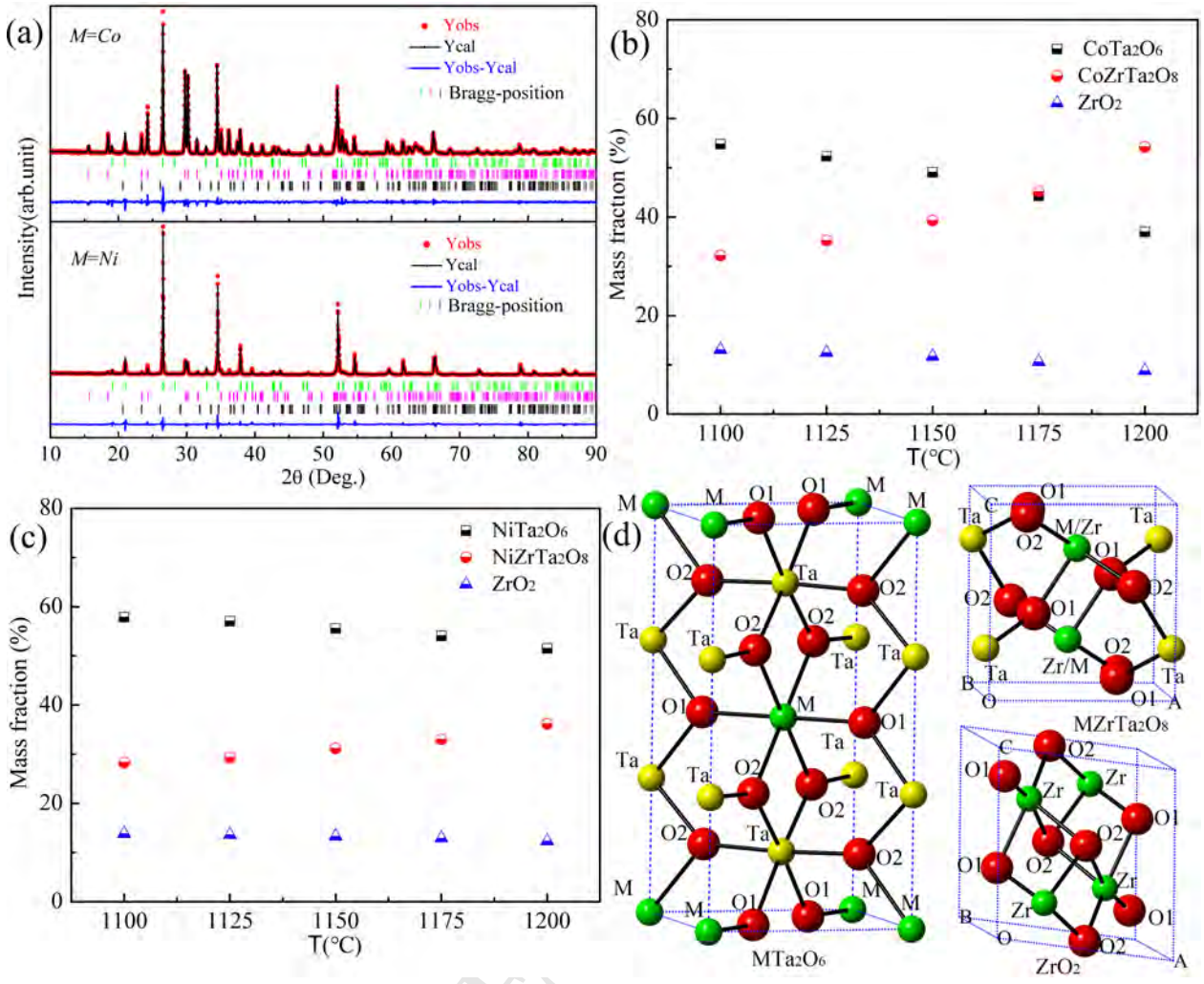
(a)
M=Co
Yobs
Ycal
Yobs-Ycal
Bragg-position
M=Ni
Yobs
Ycal
Yobs-Ycal
Bragg-position
Intensity(arb.unit)
2θ (Deg.)
(b)
CoTa2O6
CoZrTa2O8
ZrO2
Mass fraction (%)
T(°C)
(c)
NiTa2O6
NiZrTa2O8
ZrO2
Mass fraction (%)
T(°C)
(d)
MTa2O6
MZrTa2O8
ZrO2

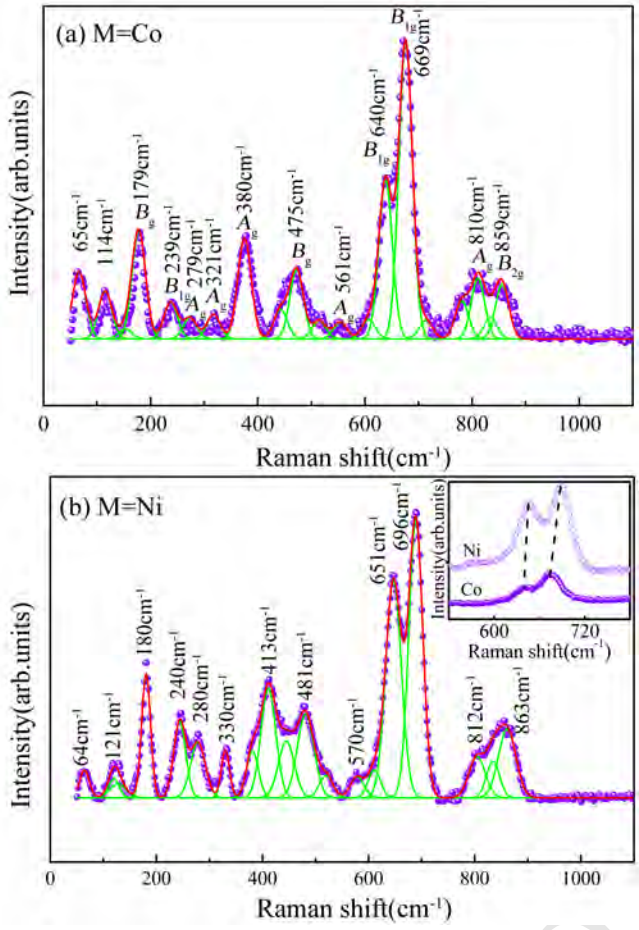

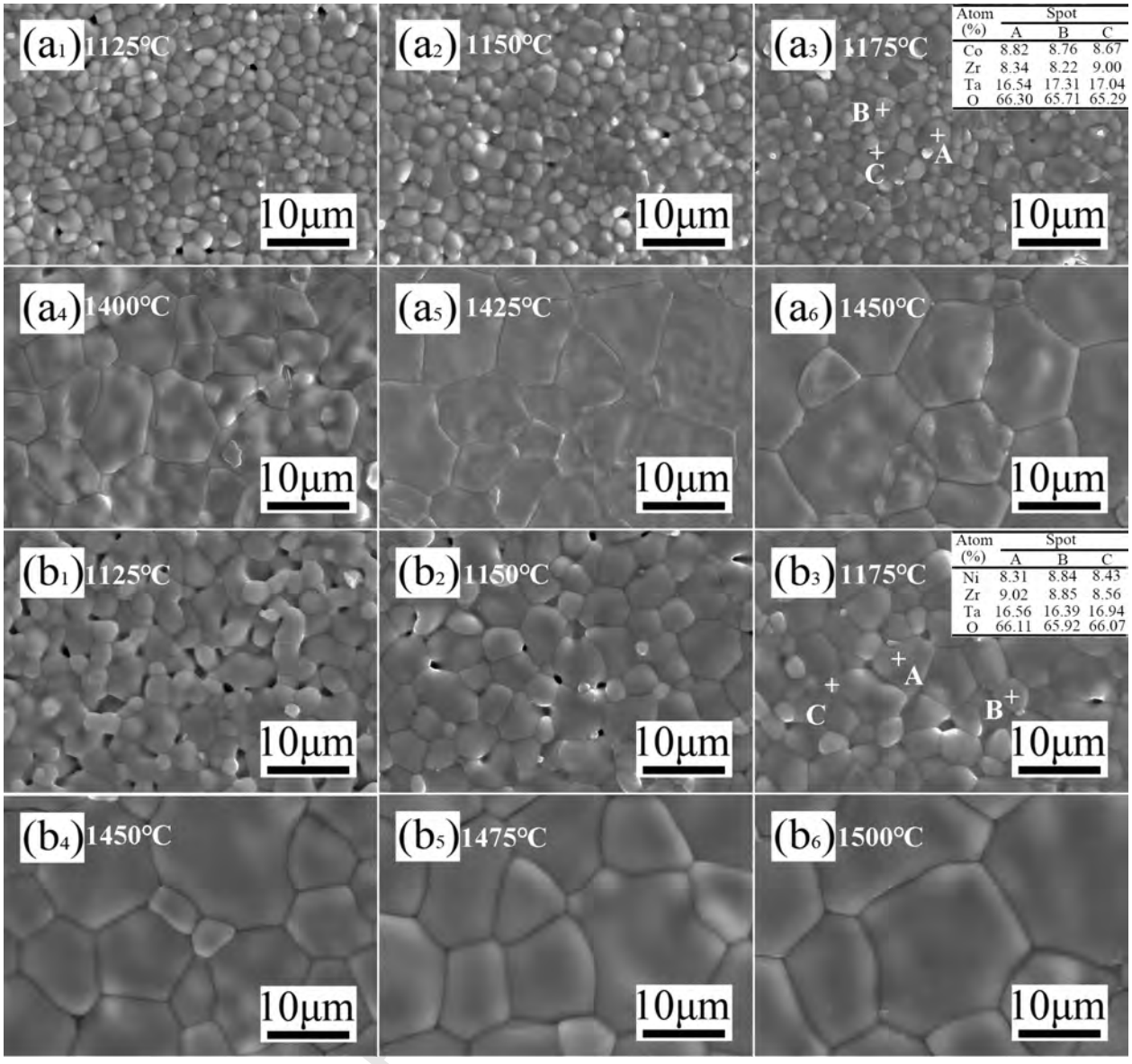

Atom (%)	Spot A	Spot B	Spot C
Co	8.82	8.76	8.67
Zr	8.34	8.22	9.00
Ta	16.54	17.31	17.04
O	66.30	65.71	65.29

Atom (%)	Spot A	Spot B	Spot C
Ni	8.31	8.84	8.43
Zr	9.02	8.85	8.56
Ta	16.56	16.39	16.94
O	66.11	65.92	66.07

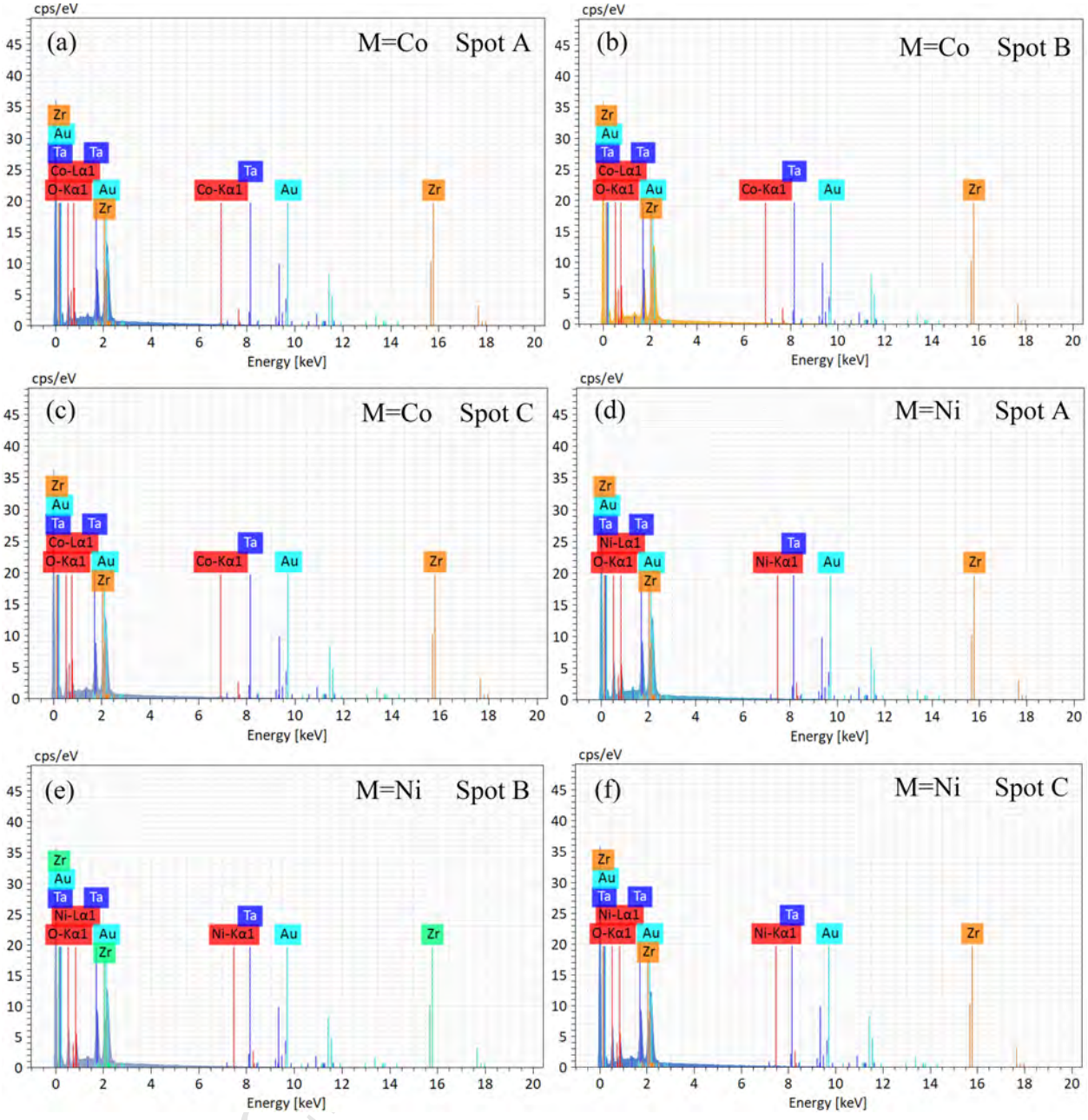
(a)
M=Co Spot A
(b)
M=Co Spot B
(c)
M=Co Spot C
(d)
M=Ni Spot A
(e)
M=Ni Spot B
(f)
M=Ni Spot C
cps/eV
Energy [keV]
Zr
Au
Ta
Co-Lα1
O-Kα1
Co-Kα1
Ni-Lα1
Ni-Kα1

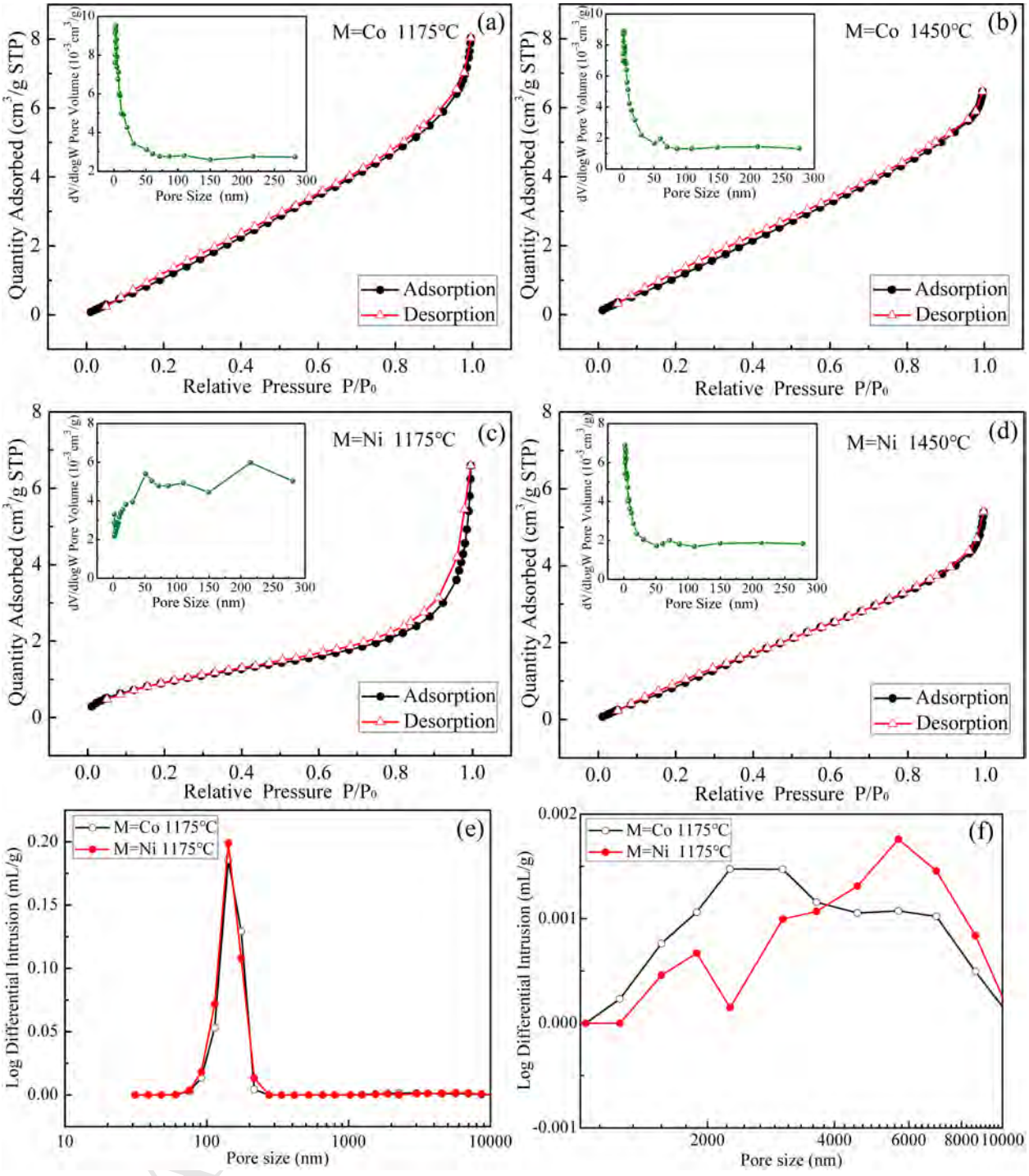
M=Co 1175°C
(a)
Quantity Adsorbed (cm³/g STP)
Relative Pressure P/P₀
Adsorption
Desorption
dV/dlogW Pore Volume (10⁻³ cm³/g)
Pore Size (nm)
M=Co 1450°C
(b)
M=Ni 1175°C
(c)
M=Ni 1450°C
(d)
M=Co 1175°C
M=Ni 1175°C
(e)
Log Differential Intrusion (mL/g)
Pore size (nm)
(f)

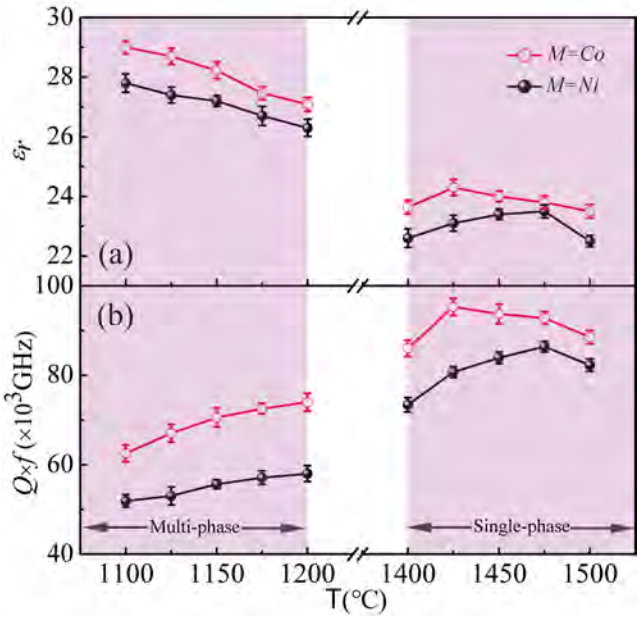

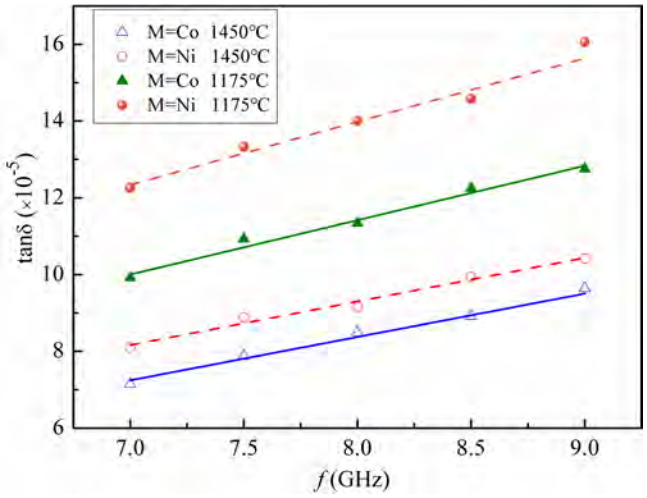

The ε_r~24.3, $Q\times f$~95,300 GHz, and τ_f~-30.50 ppm/°C were gained for $CoZrTa_2O_8$.

The $NiZrTa_2O_8$ ceramic had ε_r=23.5, $Q\times f$=86,404 GHz, and τ_f=-20.20 ppm/°C.

Near zero τ_f values were obtained for MO-ZrO_2-Ta_2O_5 composite materials.